МІНЕРАЛОГІЯ, ГЕОХІМІЯ ТА ПЕТРОГРАФІЯ

UDC 622.41
DOI: http://doi.org/10.17721/1728-2713.112.07

Victor YUROV[1], DSc (Engin.), Prof.
ORCID ID: 0000-0002-7918-9656
e-mail: s.imanbaeva1@ktu.edu.kz

Vasily PORTNOV[2], DSc (Engin.), Prof.
ORCID ID: 0000-0002-4940-3156
e-mail: v.portnov@ktu.edu.kz

Serhii VYZHVA[3], DSc (Geol.), Prof., Corresponding Member of the NAS of Ukraine
ORCID ID: 0000-0003-4091-6649
e-mail: s.vyzhva@knu.ua

Mykola REVA[3], PhD (Phys.-Math.), Assoc. Prof.
ORCID ID: 0009-0009-1307-7617
e-mail: mvreva@gmail.com

Kanat ZHANGOZIN[2,4], PhD (Phys. & Math.), Assoc. Prof.
ORCID ID: 0000-0003-1234-0486
e-mail: s.asylzat@ktu.edu.kz

Andrey GOLIK[2], PhD Student
ORCID ID: 0009-0008-5179-0002
e-mail: andrey.golik@i-geo.kz

[1]LLP "TSK-Vostok", Karaganda, Kazakhstan
[2]Saginov Karaganda Technical University, Karaganda, Kazakhstan
[3]Taras Shevchenko National University of Kyiv, Kyiv, Ukraine
[4]LLP "Vostok", Astana, Kazakhstan

SURFACE LAYER OF LAYERED MINERALS

(Представлено членом редакційної колегії д-ром геол. наук, доц. Олександром ШАБАТУРОЮ)

Background. *The surface layer of layered minerals such as graphite, molybdenum disulfide (MoS_2), and molybdenum diselenide ($MoSe_2$) can be regarded as an ultrathin film, with a thickness ranging from approximately 2 nm in the in-plane direction to about 6 nm along the out-of-plane axis. This film comprises three monolayers in graphite, four in MoS_2, and five in $MoSe_2$. At these dimensions, the surface layer forms a genuine two-dimensional (2D) structure, which exhibits properties distinct from those of the bulk crystal. Moreover, the individual nanolayers within this layer display unique characteristics owing to pronounced size-dependent effects. The aim of the present work is to explore the quantum structure of the surface layer in these minerals, to clarify the fundamental differences between metallic and semiconducting behavior, and to examine surface-related phenomena such as the electrical conductivity of the minerals and the conversion of deformation energy associated with surface reconstruction. Based on the representation of mineral nanolayers as quantum wires, together with the results of the authors' previous studies and findings reported in the scientific literature, the corresponding analytical calculations were carried out, enabling the achievement of the objectives formulated above.*

Results. *It has been established that as the thickness of semiconductors decreases, their electrical conductivity increases, which is opposite to the behavior observed in metals. In particular, the conductivity of the surface layer of graphite is two orders of magnitude higher, while that of molybdenum disulfide and molybdenum diselenide (MoS_2 and $MoSe_2$) is four orders of magnitude higher than the conductivity of the bulk phase of these minerals. It was also revealed that, in terms of its electronic properties, graphene occupies an intermediate position precisely between conventional metals and semiconductors. The paper demonstrates that quantum wires within a nanolayer interact with each other, which corresponds to the quantum entanglement of fermions as a spin system. It has been established that the deformation energy associated with the reconstruction of mineral surfaces determines the physical properties of both the nanolayers and the bulk crystal. Knowledge of this energy provides a basis for analyzing such physical properties as the thermoelectromotive force (thermocouple effect), thermoelectric effects (Seebeck, Peltier, Thomson), electron work function, heat capacity, and others. The transformation of deformation energy into various forms of energy is considered. It is shown that, under external influence, deformation energy is expended on acoustoemission (the propagation of acoustic waves), autoelectron emission (the release of slow electrons), fractoluminescence, and heat release (through friction).*

Conclusions. *The surface nanoscale layer R(l) of minerals represents an open quantum system in which quantum size effects manifest, giving rise to anomalous physical phenomena. The deformation energy arising in minerals during surface reconstruction reflects all essential properties of bulk minerals that are of significant practical relevance: the acoustic properties of materials, required for nondestructive quality control and identification of failure mechanisms; the field emission of charge carriers from metallic and semiconducting structures, which is critical for micro- and nanoelectronics, photonics, and other technological applications; the process of fractoluminescence in minerals, which reveals the mechanisms of friction in layered minerals and potential routes toward imparting them with superlubricating properties. This list of practical applications associated with deformation energy generated in minerals during surface reconstruction can be further extended. Thus, a new direction in scientific research is emerging – the physics of the surface layer of solids and liquids (in particular, for water, R(l)=1.1 nm).*

Keywords: *mineral, surface layer, nanolayer, mesolayer, bulk phase, conductivity, quantum wires, deformation energy, Fermi energy.*

ISSN 1728-3817

Background

Problem Statement. J. Gibbs represented the surface of a solid body as a geometrical plane with no thickness (Gibbs, 1928). However, Van der Waals (Van der Waals, 1893) and Guggenheim (Guggenheim, 1967) considered the surface layer as a layer of finite thickness, the magnitude of which was empirically determined in the work of (Portnov, Yurov, & Maussymbayeva, 2018; Portnov et al., 2021). According to modern understanding, the surface layer is an ultrathin film in thermodynamic equilibrium with the bulk of the crystal (Luth, 2014). Experimentally, the thickness of this film was first measured at the end of the 20th century in ultrahigh vacuum using grazing-incidence X-ray/synchrotron radiation (for example, the thickness of the surface layer was found to be 3.2 nm for silicon and 1.2 nm for gold) (Bracco, & Holst, 2013). Of particular importance is the study of the quantum structure of minerals such as graphite (C), molybdenum disulfide (MoS_2), and molybdenum diselenide ($MoSe_2$), whose surface layer is an ultrathin film ranging from ~2 nm in the in-plane direction of the layers to ~6 nm in the direction perpendicular to them. The thickness of the surface layer of these minerals determines all of their key physical properties.

Analysis of Publications on the Research Topic. For natural graphite, it is preferable to use the recent review by (Yadav, Sharma A., & Sharma S., 2025), which provides a comprehensive bibliography of previous studies. Regarding graphene (a monolayer of graphite), among the numerous publications, the monograph by (Zhang, 2022) stands out, where the properties of graphene are described. New properties of graphite are discussed in the works of (Yurov, & Zhangozin, 2023d; 2024c) and (Yurov, Zhangozhin, & Kargin, 2025b), while those of graphene are presented in the studies of (Yurov, & Zhangozin, 2023c; 2024d) and (Yurov et al., 2025d). The properties of natural molybdenum disulfide (MoS_2), also known as the mineral molybdenite, are summarized in the review by (Li S. et al., 2018). For molybdenum diselenide ($MoSe_2$), preference should be given to the review by (Wazir et al., 2022), which contains an extensive bibliography.

Identification of Previously Unresolved Aspects of the General Problem. Since the thickness of the surface layer in the mentioned minerals determines all the properties of the bulk crystal, especially at the nanoscale, it becomes relevant to address the following questions:

1) How many monolayers constitute the surface layer of a mineral, and in what respects do its properties differ from those of the bulk crystal?

2) What are the fundamental distinctions between metals and semiconductors?

3) What is the quantum structure of the surface layer in these minerals?

4) What is the origin of the anomalous effects observed in an open quantum system?

5) How is the deformation energy, associated with surface reconstruction of the given minerals, dissipated or utilized?

Research Objective. In this article, the authors aim to address the above-mentioned questions, thereby opening the possibility for a more comprehensive utilization of the unique properties of these minerals (and beyond).

Results

1) Description of the model used. We briefly present the model described in the work (Yurov et al., 2023b). For the thickness of the surface layer $R(\mathrm{I})$, the following formula is applied:

$$R(\mathrm{I}) = \alpha \cdot \upsilon, \ (\mathrm{m}), \tag{1}$$

where $\alpha=0.17\times10^{-9}$ mol/m^2; $\upsilon=M/\rho$ (M – molar mass, ρ – density) is the molar volume of the element.

The schematic of the solid is shown in Fig. 1.

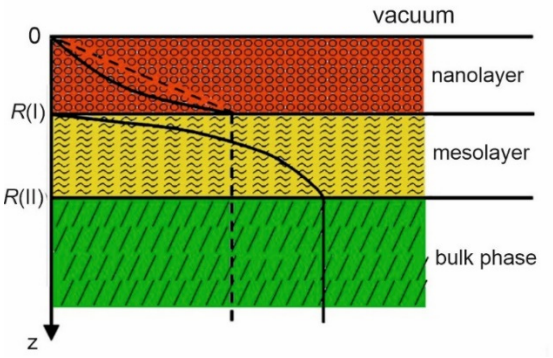

Fig. 1. Schematic of a solid: nanolayer → mesolayer → bulk phase (Yurov et al., 2023b)

The difference between the $R(\mathrm{I})$ and $R(\mathrm{II})$ phases lies in the distinct nature of size effects. In this work, we focus on the $R(\mathrm{I})$ layer. To separate the $R(\mathrm{I})$ layer from the rest of the crystal, it is necessary to expend the crystal's adhesion energy, the surface density of which W_a (specific surface energy) is given by:

$$W_a = \gamma_1 + \gamma_2 - \gamma_{12} = \beta \cdot T_m, \tag{2}$$

where γ_1, γ_2, and γ_{12} is the specific surface energies of the crystal nanolayers and the interlayer surface (γ_{12}=0); $\beta=1.1\times10^{-3}$ J/(m²·K) = const; T_m is the melting temperature (K). Here, $\gamma_1 = 0.5\gamma_2$ (see Fig. 1 and formula 5 below), and γ_{12}=0 due to a second-order phase transition (according to Ehrenfest). The $R(\mathrm{I})$ nanolayer is subject to surface reconstruction (Fig. 2).

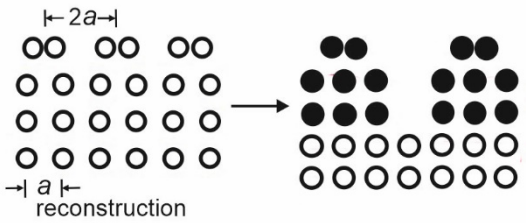

Fig. 2. Transformation of the *R*(I) layer

In this regard, internal stresses σ_{is} arise at the interphase boundary:

$$\sigma_{is} = \sqrt{W_a \cdot E \,/\, R(\mathrm{I})}, \tag{3}$$

where ***E*** is the Young's modulus.

These stresses lead to a deformation, the energy of which E_d is equal to

$$E_d = W_a \cdot a^2, \tag{4}$$

where ***a*** is the lattice constant.

The size effects in the nanolayer $R(\mathrm{I})$ and in the mesolayer $R(\mathrm{II})$ lead to the following relationships being satisfied:

$$\begin{aligned} A(z) &= A(\infty)\cdot\left[1-\frac{R(\mathrm{I})}{R(\mathrm{I})+z}\right], \quad 0 \le z \le R(\mathrm{I}), \\ A(z) &= A(\infty)\cdot\left[1-\frac{R(\mathrm{I})}{z}\right], \quad R(\mathrm{I}) \le z \le R(\mathrm{II}), \\ A(z) &= A(\infty) = \mathrm{const}, \qquad\qquad z > R(\mathrm{II}). \end{aligned} \tag{5}$$

The first equation holds for the nanolayer, the second for the mesolayer, and the third for the bulk phase.

Due to the presence of size effects in the nanolayer of a collective type (Maussymbayeva et al., 2024), the $R(\mathrm{I})$ layer can be interpreted as a nonlinear capacitor, whose circuit

diagram is shown in Fig. 3(a), and its volt-ampere characteristic (VAC) in Fig. 3(b).

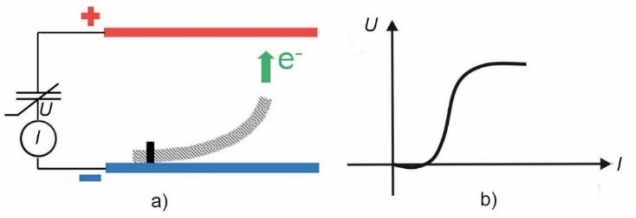

Fig. 3. Diode model of the *R*(I) layer (a) and volt-ampere characteristic of the *R*(I) layer model (b)

2) *The number of monolayers in the surface layer of graphite, MoS_2, and $MoSe_2$ minerals.* Using Eq. (1) and reference data for the molar mass M and density ρ of the minerals considered, we calculate the layer thicknesses R(I) and present the resulting values in Table 1. Using equation (1) and reference data on the molar mass M and density ρ of the specified minerals, we compute the thickness of the R(I) layer and present the values in Tab. 1.

Table 1

Thickness of the mineral nanolayer along different planes (*a=b, z=c*)

Mineral	*M*, g/mol	ρ, g/cm³	$R(I)_a$, nm	$R(I)_c$, nm
Graphite	12.0107	2.26	0.90 (3)	2.46 (3)
MoS_2	160.07	5.06	1.93 (4)	5.38 (4)
$MoSe_2$	253.86	6.90	2.29 (5)	6.25 (5)

**Note:* the *c*/*a* ratios are used here

Tab. 1 shows in brackets the number of monolayers of the surface layer of minerals, designated by the number $n=R(I)/a$ (a is the lattice constant). For natural graphite n=3, for MoS_2 – n=4 and for $MoSe_2$ – n=5.

Fig. 4 shows the experimental Raman and luminescence spectra of minerals, which indicate that above 3, 4 and 5 layers their spectra coincide with the spectra of bulk crystals of graphite, molybdenum disulfides and diselenides. This indicates the validity of the model described by equation (1).

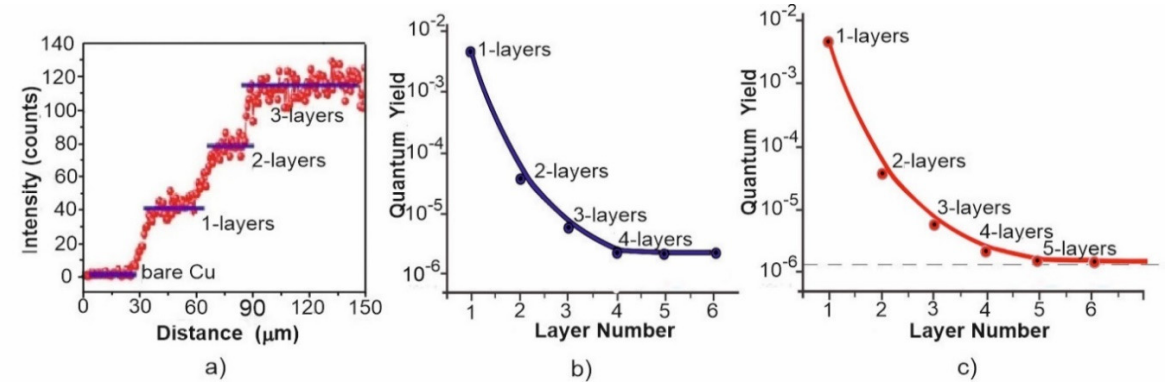

Fig. 4. Properties of Multilayer Nanostructures: Raman spectrum of graphite (a) (Abidi et al., 2018); dependence of the luminescence quantum yield of MoS_2 (b) (Eda et al., 2011) and $MoSe_2$ (c) (Tongay et al., 2012)

Figure 4 also shows that each monolayer differs from the other in physical properties. Let us briefly describe a graphite monolayer, called graphene and discovered in 2004. The presence of strong covalent σ-bonds c-c in the plane of the graphene sheet in combination with π-electrons outside it determines the unique physicochemical properties of graphene. It is characterized by a large theoretical specific surface area (≈2600 m²/g), high charge carrier mobility (≈200,000 cm²/(V·s)), high Young's modulus (≈1000 GPa), thermal conductivity (≈5000 W/(m·K)), optical transparency (≈97.7%), as well as outstanding mechanical strength, chemical stability, and other remarkable properties. Bilayer graphene differs from single-layer graphene and graphite and demonstrates improved physical, chemical, electronic and optical properties compared to graphene and bulk graphite material. Three-layer graphene differs from the last two in mobility, conductivity and magnetic properties (Devakul et al., 2023).

MoS_2 and $MoSe_2$ crystals are semiconductors because their dz^2 - bands are completely filled. Fig. 4(b) and 4(c) show the dependence of the quantum yield of luminescence of MoS_2 and $MoSe_2$ on the number of layers. The same dependences should be observed for all physical properties according to formulas (5).

Using reference data for the melting temperature T_m and Young's modulus E of the minerals, as well as the lattice constants a and c, we calculate the elastic constants of the mineral nanolayer according to equations (2) – (4): the surface adhesion energy W_a, the internal stresses σ_{is} and the deformation energy E_d. The results are presented in Tab. 2.

Table 2

Elastic constants of the minerals along different planes (*a=b, z=c*)

Mineral	W_{aa}, J/m²	W_{ac}, J/m²	σ_{isa}, GPa	σ_{isc}, GPa	E_{da}, eV (nm)	E_{dc} eV (nm)
Graphite	2.85	1.69	56.3	1.4	1.08, (a = 0.246)	4.75, (c = 0.671)
Graphene	3.45	–	118.4	–	1.30, (a = 0.246)	–
MoS_2	1.60	0.23	13.96	0.6	1.00, (a = 0.316)	4.84, (c = 1.837)
$MoSe_2$	1.62	0.42	11.3	0.7	1.08, (a = 0.328)	4.37, (c = 1.292)

**Note:* the *c*/*a* ratios are used here

From Tab. 2 it follows that high internal stresses are observed in graphene, leading to its warping and formation of corrugations (Fig. 5(a)) (Yurov et al., 2025e). Monolayers of MoS_2 and $MoSe_2$ are less deformed due to their structure (Fig. 5(b)), although warping is also observed in them (Gordon et al., 2002).

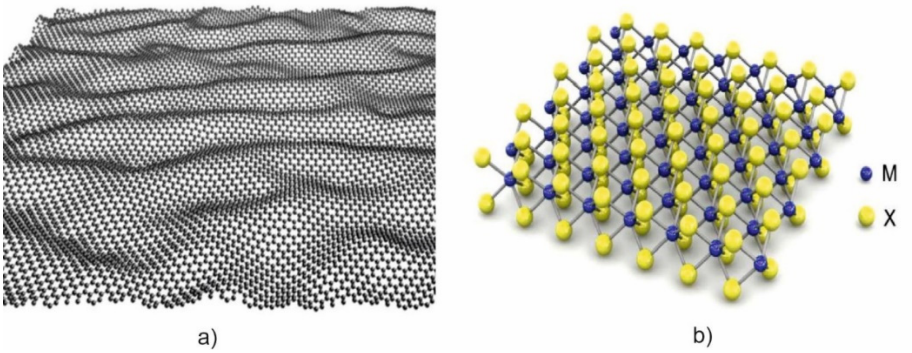

Fig. 5. Corrugated graphene (a) (Yurov et al., 2025e) and three-dimensional schematic representation of one layer of a typical MX_2 structure (b) (Phalswal et al., 2002).

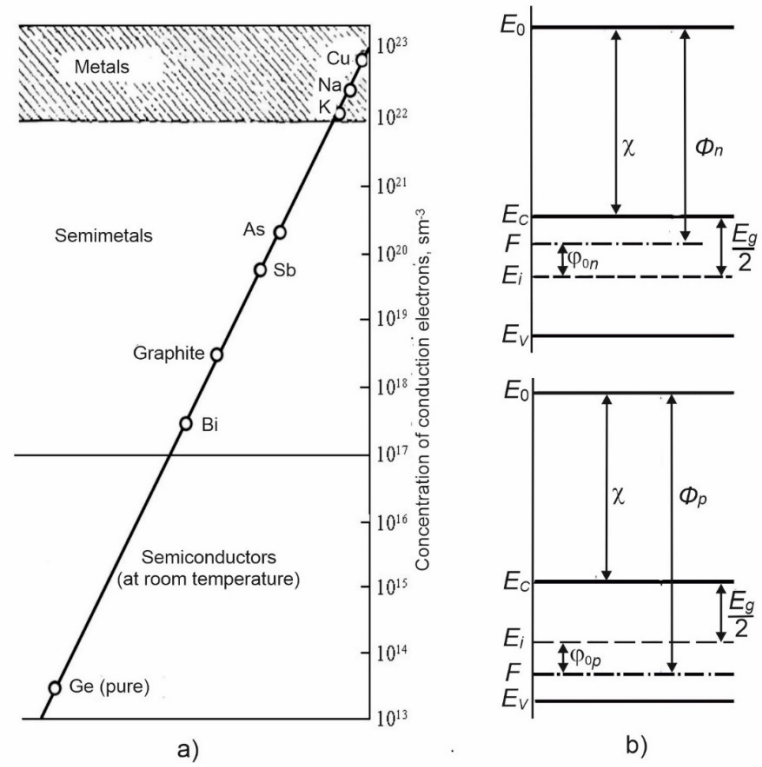

Fig. 6. Conduction electron concentrations in metals and semiconductors (a); band diagrams of semiconductors (b): top – n-type, bottom – p-type.

3) *Distinction between Metals and Semiconductors.* Metals differ from other substances in that, at T=0 K, they possess free conduction electrons (due to the presence of a partially filled energy band). All other substances at T=0 K are dielectrics (with either completely filled or completely empty energy bands). At $T > 0$ K, there is a probability for electrons to transition from the valence band to the conduction band. As a numerical estimate, one may cite the concentration of free charge carriers at room temperature: in good metals it is about $10^{22}…10^{23}$ cm^{-3}, in semimetals above 10^{17} cm^{-3}, in "good" dielectrics below 10^{10} cm^{-3}, and in semiconductors typically from 10^{13} cm^{-3} to 10^{17} cm^{-3} (Fig. 6(a)). In metals, the Fermi level lies within the conduction band, whereas in chemically pure semiconductor materials it is located near the middle of the band gap (Fig. 6(b)).

In metals, the charge carriers are electrons, whereas in semiconductors there exist carriers of both signs, namely electrons and holes, which may also differ in their effective masses. If the Fermi level is measured from the bottom of the conduction band, we obtain the following formula:

$$E_F = \frac{\Delta E_g}{2} - \frac{3}{4} k \cdot T \cdot \ln \frac{m_p^*}{m_n^*}, \quad (6)$$

where E_F is the Fermi level; $\Delta E_g = E_C - E_V$ is the band gap width (E_C, E_V – conduction and valence bands, respectively); k is the Boltzmann constant; T is the temperature; m_p^* and m_n^* are the effective masses of holes and electrons, respectively.

For semiconductors at temperatures $T > 200$ K, the value of ΔE_g is equal to:

$$\Delta E_g = \Delta E_{g\beta} - \alpha T, \quad (7)$$

where $\Delta E_{g\beta}$ is the extrapolated term, α is the temperature coefficient.

Tab. 3 presents the values of the band gap width of the minerals (ΔE_g) and the electrons work function from the minerals (E_W).

Table 3

Values of the band gap width and the electron work function of the minerals

Mineral	ΔE_g, eV	E_W, eV
Graphite	0.135	4.60 – 4.70
MoS_2	1.30 – 1.35	4.53
$MoSe_2$	0.85	?

From the comparison of Tab. 3 with Tab. 2 and Fig. 6(b), it follows that $E_{dc} \approx E_W = \Phi$ – the thermodynamic work function. In other words, unlike in metals, the Fermi energy in semiconductors (not to be confused with the Fermi level) is equal to the thermodynamic work function, but in both cases it corresponds to the chemical potential, i.e., E_F(metal) = Φ (semiconductor/dielectric) = μ = E_{dc}. For metals, this situation is illustrated in Tab. 4. Moreover, in the definition of E_F there is a considerable scatter in the literature data.

Table 4

Deformation energy E_d and Fermi energy E_F of selected metals (Yurov et al., 2025a)

Metal	E_d, (E_F), eV	Metal	E_d, (E_F), eV	Metal	E_d, (E_F) eV
Cu	7.68 (7.93)	Mo	7.16 (6.57)	Re	9.38 (10.80)
Ag	5.64 (6.15)	W	12.23 (10.42)	Fe	12.0 (12.72)
Au	6.10 (6.23)	Mn	9.73 (12.25)	Co	12.9 (13.22)
Cr	7.26 (7.80)	Tc	6.08 (9.91)	Ni	13.06 (13.22)

From the above, it follows that the deformation energy E_d ("hidden" deformation energy) determines the physical properties of both the nanolayer and the bulk crystal, i.e., it reveals a dualism – "nanolayer (mesolayer) → bulk phase". By knowing the characteristics of the bulk crystal, one can determine the structure of its nanolayer, and vice versa.

Above, we used the term "hidden" deformation energy, equal to $E_d = W_a$. A fatigue criterion was formulated based on the concept of hidden deformation energy, where it was shown that the deformation energy can be represented by a logistic function, characteristic of catastrophe theory.

P.S. Since the "hidden" deformation energy is related to the enrichment of minerals and its influence on their properties under flotation, ultrasound, laser irradiation, and other effects, it is reasonable to devote a separate article to its study. The discussion of "hidden" deformation energy continues to the present day.

4) *Quantum Structure of the Surface Layer of Graphite, MoS_2, and $MoSe_2$.* To describe the general model, we follow the works of (Yurov et al., 2024b; Yurov, Zhangozin, & Kargin, 2025c). In equation (5), the nanolayer is represented as a potential well with infinitely high walls along the z axis ($z = c$, perpendicular to the layer), while in the plane ($a = b$) the energy is continuous. Under these assumptions, the energy levels $E_n(z)$ along the z axis are given by:

$$E_n(z) = \frac{\hbar^2 \pi^2 n^2}{2 m_e R(\mathrm{I})^2}, \qquad (8)$$

where $n > 0 = 1,2,3,\ldots$; $\hbar$ is the reduced Planck constant; m_e is the electron mass.

If in equation (5) we take $A(z) = E_n$ – the energy level, then for $z \geq 0$, $E_n(z \geq 0) = E_1$, and for $z = R(\mathrm{I})$, $E_n[z = R(\mathrm{I})] = 0.5E_n(\infty) \approx 0.5\Phi \approx 0.5E_{dc} \approx 0.5E_W$. This situation is illustrated in Fig. 7.

As an example, we consider the electro-photoluminescence spectra of graphene (Fig. 8(a)) and monolayer MoS_2 and $MoSe_2$ (Fig. 8(b)).

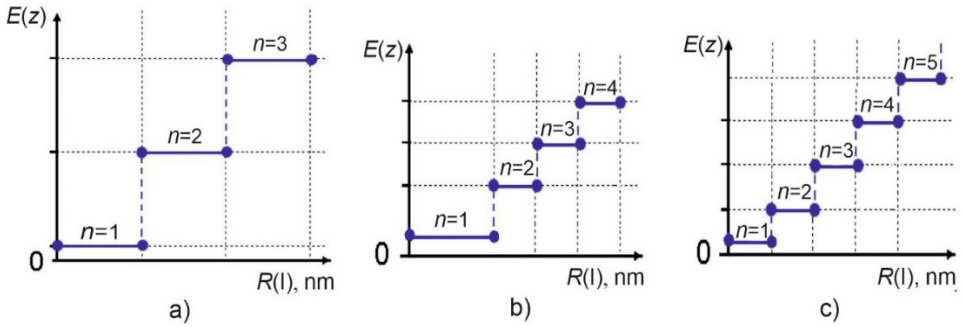

Fig. 7. Energy levels in the nanolayer of graphite (a), MoS_2 (b), and $MoSe_2$ (c)

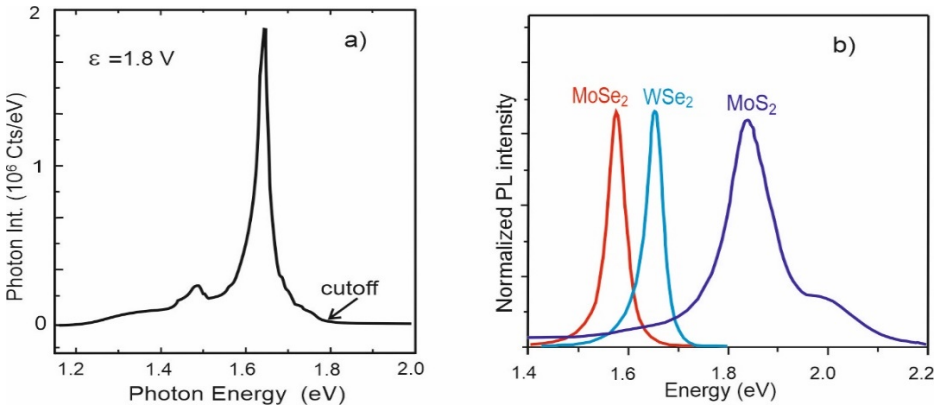

Fig. 8. Electro-photoluminescence spectra: graphene (a); monolayer MoS_2 and $MoSe_2$ (b)

From Fig. 8 it follows that the maximum intensity of electroluminescence (EL) for graphite (Fig. 8(a)) occurs at a photon energy of E_{EL}≈1.65 eV, while the maxima of photoluminescence (PL) intensity for monolayer MoS_2 and $MoSe_2$ (Fig. 8(b)) are observed at photon energies of E_{PL}≈1.85 eV and E_{PL}≈1.57 eV, respectively. These data generally correlate with the behavior of the deformation energy E_{dc} of the surfaces of these minerals (Tab. 2).

In Tables 3 and 4, a remarkable result is obtained: by knowing the deformation energy, one can determine the chemical potential not only of metals (Fermi energy) and semiconductors, but also of dielectrics, since E_d = μ – the chemical potential. Knowledge of the Fermi energy and the chemical potential provides a basis for analyzing the following physical properties: the phenomenon of thermoelectric power (thermocouple work); thermoelectric effects (Seebeck, Peltier, Thomson); the work function of electrons; heat capacity, etc. It is much easier to determine the deformation energy than the Fermi energy or the chemical potential.

5) *Origin of anomalous effects in an open quantum system.* Equation (6) is derived from the Schrödinger equation. It provides an adequate description of a potential well (or potential box) along the *z* axis, as illustrated in Fig. 7. However, its use becomes inappropriate when describing the effects of interactions between 2D materials and the external environment. In this case, the surface layer must instead be treated as an open quantum system, where the Schrödinger equation is no longer applicable and the system dynamics are governed by the Lindblad equations (Diehl et al., 2011). The evolution of the density matrix in such a framework follows an effective non-Hermitian Hamiltonian. One of the phenomena characteristic of non-Hermitian systems is the non-Hermitian skin-effect (Yao, & Wang, 2018), in which most eigenstates of a non-Hermitian operator become localized at the boundaries. This, in turn, implies a non-Bloch bulk–boundary correspondence (Kunst et al., 2018) and the development of a non-Bloch band theory based on a generalized Brillouin zone (Deng, & Yi, 2019). In the present work, we consider the bulk-interface boundary in layered minerals, where a deformation zone is formed with its associated energy E_d (Tab. 2).

In the *R*(I) nanolayer, anomalous effects occur. Among them, we note the violation of the Wiedemann-Franz (WF) law, which was established empirically in 1853 and relates three parameters of a metal and a semiconductor – the electrical conductivity and thermal diffusivity coefficients with the temperature and looks as follows (Ashcroft, & Mermin, 1976):

$$L_0 = \lambda/(\sigma \cdot T), \quad (9)$$

where L_0 is the Lorenz number (L_0=2.44×10^{-8} W·Ω/K^2 for a metal; L_0=1.47×10^{-8} W·Ω/K^2 for a semiconductor); λ is the thermal conductivity coefficient (W/(m·K)); σ is the electrical conductivity (Ω^{-1}·m^{-1}); *T* is the temperature (K).

The violation of the WF law has been addressed in numerous studies and continues to be an active area of research. In the work by (Yurov, Goncharenko, & Oleshko, 2024a), the breakdown of the WF law is attributed to the topological nature of the wave function responsible for electron transport in metals. As an example, the antiferromagnet Mn_3Ge was considered (Casian, 2010). It was shown that over a wide temperature range (0.5 K < *T* < 100 K), the Lorenz number L_0 remains constant, whereas deviations from the WF law emerge at *T* >100 K. It is believed that at high temperatures, a competition arises between thermal effects and the Berry curvature distribution. The Berry curvature of electrons gives rise to anomalous Hall, Nernst, and Righi-Leduc effects.

If the physical property *A*(z) is taken to be the parameters of a metal or semiconductor – namely, the electrical conductivity σ, the thermal conductivity λ, and the temperature *T* appearing in equation (5), then the Lorenz number in the nanolayer *R*(I) is given:

$$L(z) = L_0 \cdot \left[1 - \frac{R(\mathrm{I})}{R(\mathrm{I}) + z}\right], \quad (10)$$

where L_0=$L(\infty)$ is the Lorenz number of the bulk phase.

At *z* = 0, *L*(*z*) = 0, and at *z* = *R*(I), *L*(*z*) = 0.5 $L(\infty)$ = 0.5 L_0. At the bulk–interface boundary and below, the Lorenz number decreases in a stepwise manner (Yurov, Goncharenko, & Oleshko, 2024a), eventually reaching zero. A decrease of the Lorenz number following $L_0 \sim 1/R(\mathrm{I})$ has been observed in electrically conductive quasi-one-dimensional nanostructured organic crystals, as reported by (Casian, 2010). From equation (1), it follows that the thickness of the *R*(I) layer is proportional to the molar mass *M*, which is large for conductive organic crystals, as demonstrated by the results of Casian (2010).

From Tab. 1 and Fig. 4, it follows that the nanolayer of the minerals consists of 3 to 5 monolayers, which can be interpreted as quantum wires. Fig. 9 shows the density of states *g* in 3D-, 2D-, and 1D-structures of a metal or semiconductor, while Fig. 10 illustrates the number of quantum wires in graphite, MoS_2, and $MoSe_2$.

The conductivity of a quantum wire is given by the equation (Malet et al., 2005):

$$\sigma = \mathbf{e}^2 N/h, \quad (11)$$

where **e** is the electron charge; *N*(1/m) is the charge carrier concentration; *h* is the Planck constant.

The concentration of charge carriers *n* is determined by the Fermi energy $E_F \approx E_d = \Phi$:

$$n = \frac{8\pi}{3}\left(\frac{2m}{\hbar^2}\right)^{3/2} \cdot E_F^{3/2}, \quad (12)$$

where *m* is the mass of charge carriers, $\hbar = h/2\pi$ is the reduced Planck constant. The concentration of charge carriers in a one-dimensional structure is $N = n^{1/3}$.

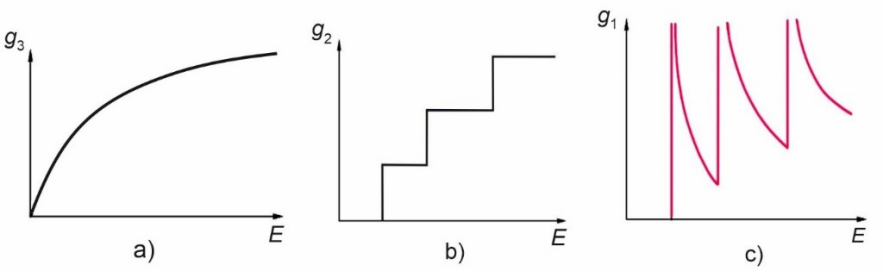

Fig. 9. Density of states in a three-dimensional metal or semiconductor (a), in two-dimensional electronic structures – quantum wells (b), and in one-dimensional structures – quantum wires (c).

Fig. 10. Number of quantum wires in graphite, MoS_2, and $MoSe_2$.

Figure 11 shows the band structure of a single sheet of graphite, i.e., graphene, from which it follows that the Fermi energy $E_F = 0$.

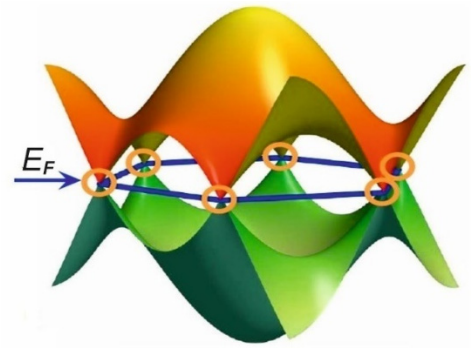

Fig. 11. Band structure of graphene

Using the data from Tables 2 and 3 and Fig. 6, we calculated the values of *n* and σ for monolayer and multilayer minerals, with the results summarized in Tab. 5. For comparison, the table also includes literature-reported electrical conductivity values of bulk minerals: graphite, MoS_2, and $MoSe_2$.

From the comparison of the electrical conductivities presented in Tab. 5, it follows that as the thickness of the semiconductor decreases, the conductivity σ increases by approximately two orders of magnitude for graphite and about four orders of magnitude for MoS_2 and $MoSe_2$. This trend is opposite to the behavior observed in metals (Fig. 12).

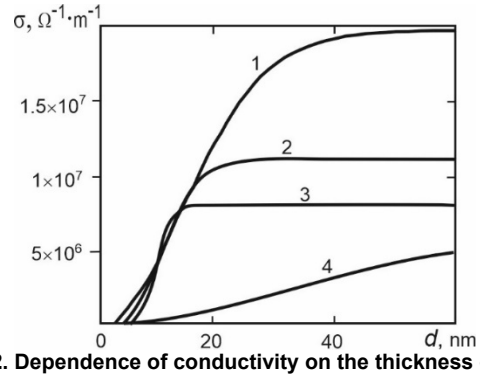

Fig. 12. Dependence of conductivity on the thickness of films of various metals (Antonets et al., 2004):
1 – silver; 2 – copper; 3 – gold;
4 – iron (conductivity increased fivefold)

The behavior of electrical conductivity in semiconductors is illustrated in Fig. 13, adapted from (Mendez, & Mamaluy, 2022). It can be seen that for silicon, as the layer thickness decreases, the conductivity increases from 10^4 to 10^7 $\Omega^{-1}\cdot m^{-1}$.

The diode model of the R(I) layer, shown in Fig. 3, corresponds to a metal, whereas its display corresponds to a semiconductor (Fig. 14).

Table 5

Specific electrical conductivity of monolayer, multilayer, and bulk minerals

Mineral	Monolayer and multilayer minerals			Bulk (massive) minerals
	n, m^{-1}		σ_n, $\Omega^{-1}\cdot m^{-1}$	**σ**, $\Omega^{-1}\cdot m^{-1}$
Graphite	$n_1=6\times10^{11}$	$n_3=1.05\times10^{12}$	$\sigma_3=4.2\times10^7$	1.13×10^5 (Deprez, & McLachlan,1988)
MoS_2	$n_1=2.91\times10^9$	$n_4=3.70\times10^9$	$\sigma_4=1.48\times10^5$	26.4 (Thakurta, & Dutta, 1983)
$MoSe_2$	$n_1=9.32\times10^9$	$n_5=11.84\times10^9$	$\sigma_5=4.73\times10^5$	42.1 (Zhong et al., 2021)

**Note*: *n* – Charge carrier concentration

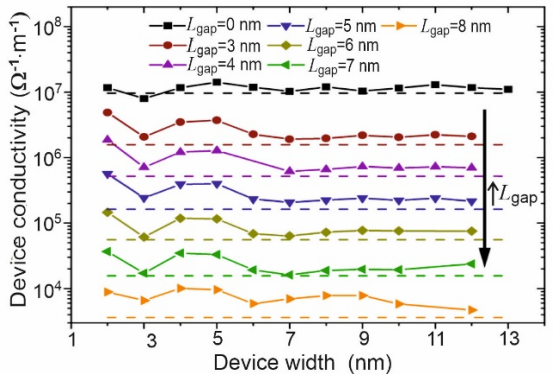

Fig. 13. Electrical conductivity of multilayer silicon (Si) (Mendez, & Mamaluy, 2022): L_{gap} – layer thickness

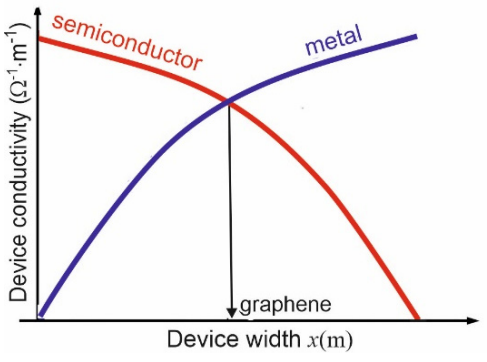

Fig.14. Dependence of conductivity on layer thickness for a metal and a semiconductor

From Fig. 14 it can be seen that, in terms of its electronic characteristics, graphene occupies an intermediate position between conventional metals and semiconductors. This is explained by its unique nature: graphene is a two-dimensional metal whose electronic spectrum is characterized by linear dispersion and is described by a massless Dirac Hamiltonian.

The quantum wires in Fig. 10 represent fermions with half-integer spin and are regarded as a spin ladder (the valley effect is neglected). Such spin ladders began to be investigated experimentally in the 1990-s (Dagotto, Riera, & Scalapino, 1992), although the one-dimensional model was originally proposed by Ising in 1925 (Ising, 1925).

The Tomonaga-Luttinger model, which is universal for one-dimensional electronic and spin systems (Tomonaga, 1950; Luttinger, 1963), can also be applied to the ladder in Fig. 10. In this context, the Tomonaga-Luttinger model allows for different ratios of exchange integrals in the spin ladder, which the authors of the present study exploit in their analysis of the Ising model.

The Ising model is defined by Eq. (13) and depicted in Fig. 15:

$$J_{\perp} = \frac{kT_N}{1.28\sqrt{\ln\frac{5.8J_{\parallel}}{kT_N}}}, \qquad (13)$$

where k is the Boltzmann constant; T_N is the spin-ordering temperature; $J_{\parallel}$ is the exchange integral along the chain; $J_{\perp}$ is the interchain interaction parameter.

In the present paper, the authors replace the exchange integral $J_{\parallel}$ with the thermodynamic work function of the quantum wire (Φ=E_d), equal to E_d/n (n – the number of monolayers along the z-axis), and the interchain interaction is taken as $J_{\perp}$=$E_d/(n-1) - E_d/n$. This procedure can be continued iteratively.

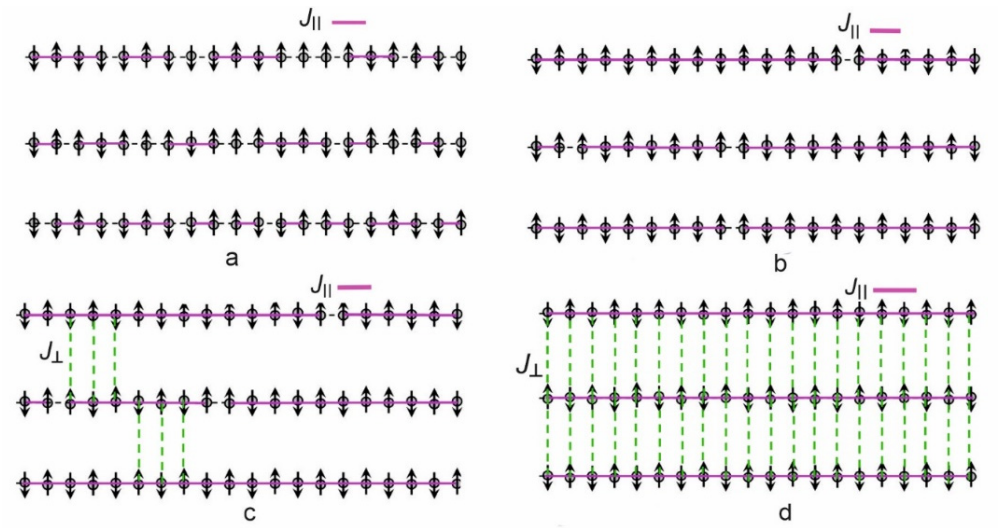

Fig. 15. $T \sim J_{\parallel}$ – correctly aligned neighboring spins appear (a);
$T \ll J_{\parallel}$ – the size of correctly ordered fragments increases, while disorder remains (b);
$T \sim J_{\perp}$ – interchain interaction becomes significant (c);
$T \ll J_{\perp}$ – phase transition to an ordered state occurs at T_N (d): (T – Mineral temperature)

Let us examine this question for the mineral MoS_2, using the value E_{dc}=4.84 eV from Tab. 2: $J_{\parallel} = E_{dc}/n = E_{dc}/4 =$ = 1.21 eV = 1.21/(8.617×10^{-5} eV/K) ≈ 14042 K < 89000 K (equal to E_F for a metal); $J_{\perp} = E_{dc}/(n\text{-}1) - E_{dc}/n$ = 1.61–1.21 = 0,4 eV ≈ 4642 K << 89000 K. These data indicate that the conditions $T \ll J_{\parallel}$ and $T \ll J_{\perp}$ are satisfied, with $J_{\parallel} > J_{\perp}$. It follows that the quantum wires interact with each other, thereby undergoing a phase transition to an ordered state, while disorder still remains (Fig. 15).

The interaction of quantum wires in the R(I) layer corresponds to the quantum entanglement of fermions as a spin system (Claser, Buttner, & Fehske, 2003). Entropy is taken as a measure of quantum entanglement (Nishioka, 2018). In the work (Yurov, Zhangosin, & Kargin, 2024f) the obtained the following expression for the value of quantum entanglement:

$$\frac{2\Delta S}{k\cdot\tau}\cdot\exp\left[\frac{E_F+(E_2-E_1)}{k\cdot T_0}\right]=1, \qquad (14a)$$

or

$$\Delta S=\frac{k\cdot\tau}{2}\exp\left[-\frac{E_F+(E_2-E_1)}{k\cdot T_0}\right]. \qquad (14b)$$

Here, ΔS is the increment of entanglement entropy; τ is the characteristic relaxation time of the spin chain (quantum wires); E_F is the Fermi energy; E_1, E_2 are the energies of the corresponding states of the quantum wires; and T_0 is the characteristic temperature (the transition temperature from disorder to the coherent phase).

According to (Nishioka, 2018), the value of ΔS=1. In this case, for MoS_2 the exchange integral $J_{\parallel}$ is equal to $E_{da}/4$=0.25 eV≈2901 K, while T_0=700 K. It should be noted that the thermal vibration energy at room temperature is ≈ 0.025 eV, i.e., an order of magnitude smaller. Quantum entanglement arises from the principle of superposition of states and plays an essential role in the development of quantum computation and quantum computers (Nielsen, & Chuang, 2010).

6) *Conversion of deformation energy into various types of energy.* First, consider the transformation of deformation energy into *acoustic emission*. Several sources of acoustic emission of metals and semiconductors are currently known: dislocation motion; crack initiation and growth; twinning process (Bruneau, & Potel, 2009). The authors add to this list – the transformation of deformation energy into acoustic emission.

Acoustic emission (AE) is the generation of extremely weak ultrasonic radiation accompanying structural changes in solids, particularly under deformation (Fig. 16).

The total acoustic emission energy E_{AE} is equal to:

$$E_{AE} = \frac{\sigma_0^2 \, \lambda \, [R(I)]^2}{8 \, \rho \, \upsilon^2}, \qquad (15)$$

where σ_0 (in our case $\sigma_0 \approx \sigma_{is}$) is the maximum amplitude of the elastic oscillation stresses; λ is the wavelength of the oscillations (in our case $\lambda = R(I)$); ρ is the density of the body; υ is the speed of sound.

The maximum wavelength λ propagating along the discrete chain in the z axis is equal to $R(I)_c$. The speed of sound in the surface layer of graphite is given by $\upsilon = R(I)/\tau$, where τ is the relaxation time. For longitudinal modes, the relaxation time is $\tau_L = 0.2\times10^{-12}$ s, and for transverse modes $\tau_T = 2\times10^{-12}$ s. For graphite and graphene, the density (ρ) and speed of sound of longitudinal (υ_L) and transverse (υ_T) modes are presented in Tab. 6.

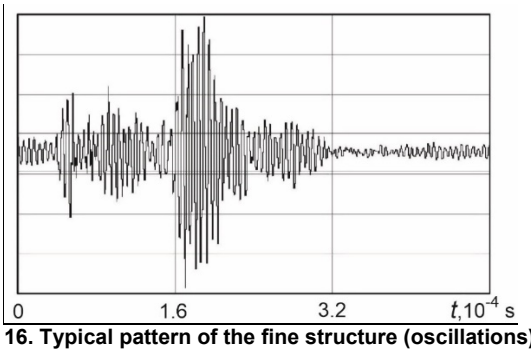

Fig. 16. Typical pattern of the fine structure (oscillations) of acoustic emission signals recorded by a sensor on the surface of the examined body

Table 6

Density and speed of sound of longitudinal and transverse modes in graphite and graphene

Mineral	ρ	υ_L, m/s	υ_T, m/s
Graphite	2260 kg/m^3	4500	2380
	1986 kg/m^3	3505	1854
	1753 kg/m^3	2631	1591
Graphene	0.77 mg/m^3	19700	10700

From Tab. 6, it can be seen that the density of graphene is significantly lower than that of graphite, yet the speed of sound in graphene is almost five times higher.

We transform Eq. (15) using Eqs. (1) – (4) and the expressions from (Abidi et al., 2018). As a result, we obtain:

$$E_{AE} = \beta \frac{T_m \cdot E \cdot R(I)}{M}, \ (\text{eV}), \qquad (16)$$

where β=0.2 eV·kg/(K·Pa·m); T_m is the Melting temperature of the solid (K); E is the Young's modulus (Pa); M is the mass of the 1m^3 crystal (kg).

Let us estimate E_{AE} for graphite: with T_m=3900 K, $E \approx 4.2$ GPa, $R(I)$=2.46 nm, and $M \approx 1700$ kg, we obtain $E_{AE} \approx 4.6$ eV. Comparing this value with Tables 2 and 3, one finds that $E_{AE} \approx E_{dc} \approx E_W$ = (4.6–4.84) eV, and the deformation energy E_d of graphite, arising from surface reconstruction, coincides within experimental error with the acoustic emission energy: $E_d \approx E_{AE}$. This result demonstrates that in natural graphite, as in other solids, acoustic emission arises from surface reconstruction leading to the formation of the surface layer $R(I)$ and the associated deformation energy E_d. Thus, under external influences (laser irradiation, ultrasound, etc.) the deformation energy is converted into acoustic emission.

Formula (16) indicates that the acoustic emission energy E_{AE} is proportional to temperature, which enables the use of graphene as a thermophone – device in which thermoacoustics converts heat into sound. Such a graphene-based thermophone differs from conventional speakers and piezoelectric transducers by the complete absence of mechanically moving parts (Fig. 17).

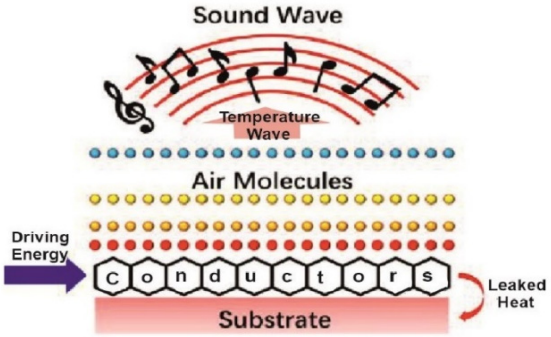

Fig. 17. Schematic of the operating principle of a thermoacoustic transducer

Our model, presented Eq. (16), contains only experimentally determined parameters, and their accuracy is quite acceptable. The acoustic emission energy in Eq. (16) is proportional to $R(I)$. In the work of (Yurov, Goncharenko, & Oleshko, 2023a), it was shown that the thickness of the surface layer $R(I)$ corresponds to the crack length L. Cracks (Fig. 18) determine the performance of all existing structures and are studied using the acoustic emission method. The addition of graphene to cement mortar significantly strengthens standard concrete (by a factor of 4–5) and reduces the number of nanocracks (Yurov, Zhangozin, & Kargin, 2024e).

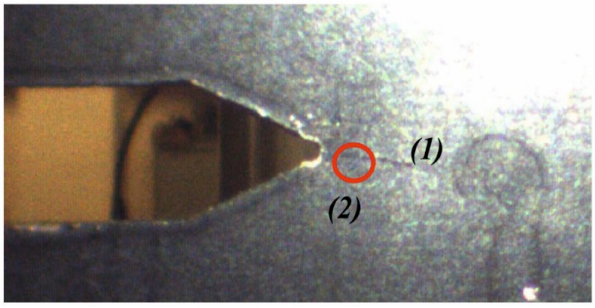

Fig. 18. Illustration of fatigue cracks: main crack (1); "secondary" cracks (2)

Let us now consider the conversion of deformation energy into *field electron emission* from metals and semiconductors. The emission of electrons from these materials is described using Fowler-Nordheim theory. According to this theory, the work performed against the forces confining an electron within the cathode can be represented by an energy diagram (Fig. 19). The corresponding formula is given by (Fursey, 2005):

$$j \approx \frac{a \cdot E^2}{\Phi} \cdot \exp\left(-\frac{b \cdot \Phi^{3/2}}{E}\right), \qquad (17)$$

where j is emission current density (A/m^2); E is local electric field at the surface (V/m); Φ is work function of the material (eV); a, b is universal Fowler-Nordheim constants, with approximate values: $a \approx 1.54\times10^{-6}$ (A·eV/m^2), $b \approx 6.83\times10^9$ (V/(m·eV$^{3/2}$)).

From Fig. 19 it follows that the total potential is the sum of the image force potential and the external potential. The current–voltage characteristic of emitter systems is of the type shown in Fig. 3(b).

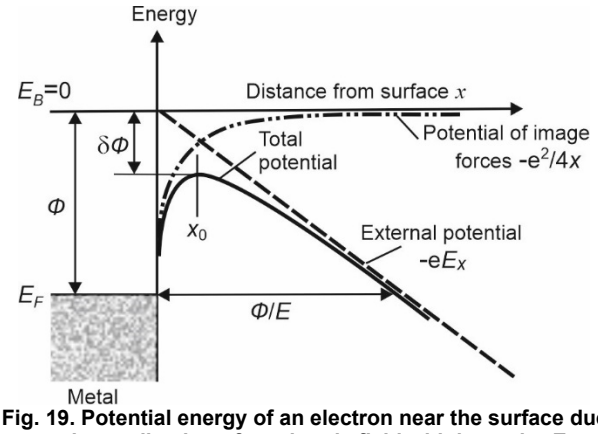

Fig. 19. Potential energy of an electron near the surface due to the application of an electric field with intensity E: (solid line – total potential; Φ – work function without the field; $\delta\Phi$ – change in the work function under the field)

The Fowler-Nordheim theory describes experimental results well for metallic and semiconductor emitters with a tip radius greater than 100 nm. However, when the emitter radius is less than 10 nm, the Fowler-Nordheim theory yields overestimated results. In our case, as shown in Tab. 1, we have R(I) < 10 nm. The work function $\Phi = E_W$ (Fig. 19) is given in Tab. 3. From Tables 3 and 2 it follows that, for the studied minerals, $\Phi \approx E_{AE} \approx E_W \approx E_{dc}$. This demonstrates that the deformation energy is expended in field electron emission.

Let us consider the conversion of deformation energy into *fractoluminescence*. Fractoluminescence (FL) is the emission of light during crystal fracture. Crystal fracture can also occur under friction, in which case the light emission is referred to as triboluminescence (TL), a term synonymous with FL. There are two main viewpoints regarding the origin of FL and TL (Moss, & Landsberg, 1992). Some authors attribute FL and TL to a gas discharge between the faces of growing cracks, while others associate them with electronically excited free radicals at the crack surfaces. To date, the discussion on the origin of FL and TL remains ongoing.

Let us assume that a part of the deformation energy is converted into fractoluminescence in minerals. We then estimate the maximum energy of the fractoluminescent emissions of the studied minerals. Table 7 presents the experimental values of the wavelengths λ_{max} corresponding to the maximum energy of fractoluminescence $(E_{FL})_{max}$ for graphite, MoS_2 (an example is shown in Fig. 20), and $MoSe_2$, obtained in the studies (Sundaram et al., 2013; Zhang et al., 2015).

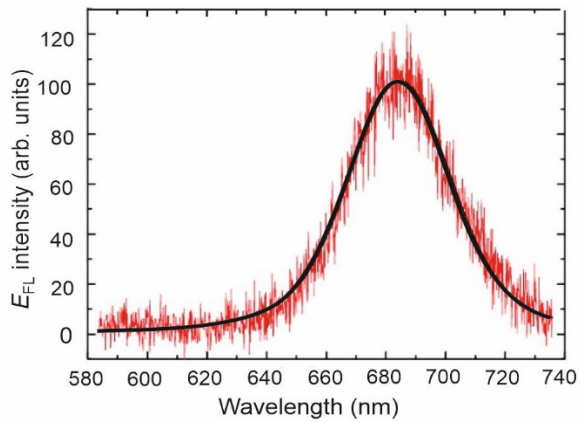

Fig. 20. Fractoluminescence of MoS_2 (Sundaram et al., 2013)

Using the relation $\lambda = h \cdot c/E_{FL} \approx 1240$ (eV·nm)/E_{FL}, where h is Planck's constant and c is the speed of light, we obtain the maximum values of the fractoluminescence energy $(E_{FL})_{max}$ for the studied minerals (Tab. 7):

Table 7

Wavelengths and maximum energy of fractoluminescent emission of minerals

Mineral	λ_{max}, nm	$(E_{FL})_{max}$, eV
Graphite	630	1.968
MoS_2	692	1.792
$MoSe_2$	764	1.623

Referring to Tab. 2, one can see that in the shear plane deformation energy $E_d \approx 1$ eV, which corresponds to the solid lubrication effect. This effect is characteristic of the minerals under study. To achieve ultralow friction (friction coefficient $k \approx 10^{-3}$–10^{-4}), and hence attain superlubricity (Liu et al., 2019), it is necessary that $E_d \ll 1$ eV. From Eq. (4), it follows that the value of E_d depends on the adhesion energy W and the lattice constant a ($a = R$(I)$/n$, where n is the number of monolayers of the mineral). Therefore, both of these parameters must be reduced. The tribological properties of graphene have been investigated in detail. As a result of that, it was concluded that the key factors influencing tribological performance are adhesion, the number of layers, stacking order, and the substrate material.

Summarizing the discussion of deformation energy conversion on mineral surfaces, it should be emphasized that the open quantum system of the surface layer R(I), when subjected to external influences such as friction, dissipates the deformation energy generated during surface reconstruction into acoustic emission, electron emission, fractoluminescence, and heat release.

Discussion and conclusions

The surface nanoscale layer R(I) of minerals represents an open quantum system in which quantum size effects manifest, giving rise to anomalous physical phenomena. The deformation energy arising in minerals during surface reconstruction reflects all essential properties of bulk minerals that are of significant practical relevance: the acoustic properties of materials, required for nondestructive quality control and identification of failure mechanisms; the field emission of charge carriers from metallic and semiconducting structures, which is critical for micro- and nanoelectronics, photonics, and other technological applications; the process of fractoluminescence in minerals, which reveals the mechanisms of friction in layered minerals and potential routes toward imparting them with superlubricating properties. This list of practical applications associated with deformation energy generated in minerals during surface reconstruction can be further extended. Thus, a new direction in scientific research is emerging – ***the physics of the surface layer of solids and liquids*** (in particular, for water, R(I)=1.1 nm).

Authors' contribution: Victor Yurov – Conceptualization, Methodology, Writing (Original Draft); Vasily Portnov – Methodology, Formal Analysis; Serhii Vyzhva – Conceptualization, Writing (Review & Editing); Mykola Reva – Data Validation, Writing (Review & Editing); Kanat Zhangozin – Software, Formal Analysis; Andrey Golik – Formal Analysis, Data Validation.

Funding Sources. This work was carried out with the support of the Science Committee of the Ministry of Science and Higher Education of the Republic of Kazakhstan within the framework of program-targeted funding for the implementation of the scientific, scientific and technical program IRN No. BR24993009.

References

Abidi, I. H., Weng, L.-T., Wong, C. P. J., Tyagi, A., Gan, L., & Ding, Y. (2018). New approach to unveiling individual atomic layers of 2D materials and their heterostructures. *Chemistry of Materials*, 30(5), 1718–1728. https://doi.org/10.1021/acs.chemmater.7b05371

Alleyne, D., & Cawley, P. (1994). The practical excitation of Lamb waves using piezoelectric transducers. *Review of Progress in QNDE*, *13*, 181–188.

Antonets, I. V., Kotov, L. N., Nekipelov, S. V., & Golubev, E. A. (2004). Features of nanostructure and specific conductivity of thin films of various metals. *Journal of Technical Physics*, 3, 24–27. https://doi.org/10.1134/1.1826197

Ashcroft, N. W., & Mermin, N. D. (1976). *Solid state physics*. Holt, Rinehart and Winston.

Beaty, K. S., Schmitt, D. R., & Sacchi, M. (2002). Simulated annealing inversion of multimode Rayleigh wave dispersion curves for geological structure. *Geophysical Journal International*, 151, 622–631. https://doi.org/10.1046/j.1365-246X.2002.01809.x

Bracco, G., & Holst, B. (2013). *Surface science techniques*. Springer-Verlag Berlin Heidelberg. https://doi.org/10.1007/978-3-642-34243-1

Bruneau, M., & Potel, C. (Eds.). (2009). *Materials and acoustics handbook*. ISTE Ltd.

Casian, A. (2010). Violation of the Wiedemann-Franz law in quasi-one-dimensional organic crystals. *Physical Review B*, 81(15), Article 155415. https://doi.org/10.1103/PhysRevB.81.155415

Chong, M. C., Afshar-Imani, N., Scheurer, F., Cardoso, C., Ferretti, A., & Prezzi, D. (2018). Bright electroluminescence from single graphene nanoribbon junctions. *Nano Letters*, 18, 175–181. https://doi.org/10.1021/acs.nanolett.7b03797

Dagotto, E., Riera, J., & Scalapino, D. (1992). Superconductivity in ladders and coupled planes. *Physical Review B*, 45(10), 5744–5747. https://doi.org/10.1103/PhysRevB.45.5744

Deng, T.-S., & Yi, W. (2019). Non-bloch topological invariants in a non-Hermitian domain wall system. *Physical Review B*, 100, Article 035102. https://doi.org/10.1103/PhysRevB.100.035102

Deprez, N., & McLachlan, D. S. (1988). Electrical conductivity of graphite powders. *Journal of Physics D: Applied Physics*, 21, 101–107. https://doi.org/10.1023/A:1023885817514

Devakul, T., Ledwith, P. J., Xia, L.-Q., Uri, A., de la Barrera, S., Jarillo-Herrero, P., & Fu, L. (2023). Magic-angle helical trilayer graphene. *Science Advances*, 9(36), Article 6063. https://hdl.handle.net/1721.1/153511

Diehl, S., Rico, E., Baranov, M. A., & Zoller, P. (2011). Topology by dissipation in atomic quantum wires. *Nature Physics*, 7, 971–986. https://doi.org/10.1038/nphys2106

Eda, G., Yamaguchi, H., Voiry, D., Fujita, T., Chen, M., & Chhowalla, M. (2011). Photoluminescence from chemically exfoliated MoS2. *Nano Letters*, 11(12), 5111–5116. https://doi.org/10.1021/nl201874w

Fursey, G. N. (2005). *Field emission in vacuum microelectronics*. Kluwer Academic.

Gibbs, J. W. (1928). *The collected works* (Vol. 1). Longmans, Green and Co.

Glaser, U., Buttner, H., & Fehske, H. (2003). Entanglement and correlation in anisotropic quantum spin systems. *Physical Review A*, 68(3), Article 032318. https://doi.org/10.1103/PhysRevA.68.032318

Gordon, R. A., Yang, D., Crozier, E. D., Jiang, D. T., & Frindt, R. F. (2002). Structures of exfoliated single layers of WS2, MoS2, and MoSe2 in aqueous suspension. *Physical Review B*, 65, Article 125407. https://doi.org/10.1103/PhysRevB.65.125407

Guggenheim, B. A. (1967). *Thermodynamics*. North-Holland Publishing Co.

Ising, E. (1925). Beitrag zur Theorie des Ferromagnetismus. *Zeitschrift fur Physik*, 31, 253–258. https://doi.org/10.1007/BF02980577

Kekana, M., Mahladisa, M., Matshaba, M., Sikhwivhilu, L., Ntsendwana, B., & Mosuang, T. (2024). Electronic and equilibrium properties of molybdenum disulphide: Density Functional Theory study. *MATEC Web of Conferences*, *406*, Article 02004. https://doi.org/10.1051/matecconf/ 202440602004

Kunst, F. K., Edvardsson, E., Budich, J. C., & Bergholtz, E. J. (2018). Biorthogonal bulk-boundary correspondence in non-Hermitian systems. *Physical Review Letters*, 121, Article 026808. https://doi.org/10.1103/PhysRevLett.121.026808

Li, S., Tang, H., Ge, P., Jiang, F., Zhou, J., Zhang, C., Hou, H., Sun, W., & Ji, X. (2018). Electrochemical investigation of natural ore molybdenite (MoS2) as a first-hand anode for lithium storages. *ACS Applied Materials & Interfaces*, 10, 6378–6389. https://doi.org/10.1021/acsami.7b18571

Liu, L., Zhou, M., Jin, L., Li, L., Mo, Y., Su, G., Li, X., Zhu, H., & Tian, Y. (2019). Recent advances in friction and lubrication of graphene and other 2D materials: Mechanisms and applications. *Friction*, 1–18. https://doi.org/10.1007/s40544-019-0268-4

Luth, H. (2014). *Surfaces and interfaces of solids*. Springer Berlin Heidelberg.

Luttinger, J. M. (1963). An exactly soluble model of a many-fermion system. *Journal of Mathematical Physics*, 4, 1154–1162. https://doi.org/10.1063/1.1704046

Mahmoodian, M., Eskandari-Ghadi, M., & Nikkhoo, A. (2020). Rayleigh, Love and Stoneley waves in a transversely isotropic saturated poroelastic media by means of potential method. *Soil Dynamics and Earthquake Engineering*, 134, 106–139. https://doi.org/10.1016/j.soildyn.2020.106139

Malet, F., Pi, M., Barranco, M., & Lipparini, E. (2005). Ground state structure and conductivity of quantum wires of infinite length and finite width. *Physical Review B*, 72(20), Article 205326. https://doi.org/10.1103/PhysRevB.72.205326

Maussymbayeva, A., Yurov, V., Portnov, V., Rabatuly, M., & Rakhimova, G. (2024). Assessment of the influence of the surface layer of coals on gass-dynamic phenomena in the coal seam. *Naukovyi Visnyk Natsionalnoho Hirnychoho Universytetu*, 2, 5–11. https://doi.org/10.33271/nvngu/2024-2/005

Mendez, J. P., & Mamaluy, D. (2022). Conductivity and size quantization effects in semiconductor δ-layer systems. *Scientific Reports*, 12, Article 1639. https://doi.org/10.1038/s41598-022-20105-x

Moss, T. S., & Landsberg, P. T. (Eds.). (1992). *Handbook on semiconductors* (Vol. 1: Basic properties of semiconductors; 2nd ed.). Elsevier.

Nielsen, M. A., & Chuang, I. (2010). *Quantum computation and quantum information*. Cambridge University Press.

Nishioka, T. (2018). Entanglement entropy: Holography and renormalization group. *Reviews of Modern Physics*, 90, Article 035007. https://doi.org/10.1103/RevModPhys.90.035007

Penkov, O. V. (2020). *Graphene. Simulation methods, preparation methods, and their applications*. Elsevier.

Phalswal, P., Khanna, P. K., Rubahn, H.-G., & Mishra, Y. K. (2022). Nanostructured molybdenum dichalcogenides: A review. *Materials Advances*, 3, 5672–5697. https://doi.org/10.1039/d2ma00150k

Portnov, V., Yurov, V., & Maussymbayeva, A. (2018). Influence of surface minerals on rebellious ore disintegration. *Journal of Mining Science*, 54(4), 681–689. https://doi.org/10.1134/S106273911804460

Portnov, V., Yurov, V., Reva, N., Mausymbaeva, A., & Imanbaeva, S. (2021). Nanostructures in the surface layers of coal matter. *Visnyk of Taras Shevchenko National University of Kyiv. Geology*, 4(95), 54-63 [in Russian]. [Портнов, В., Юров, В., Рева, М., Маусимбаєва, А., & Іманбаєва, С. (2025). Наноструктури в поверхневих шарах вугільної речовини. *Вісник Київського національного університету імені Тараса Шевченка. Геологія*, 4(95), 54-63]. https://doi.org/10.17721/1728-2713.95.07

Song, I., Park, C., & Choi, H. C. (2015). Synthesis and properties of molybdenum disulphide: From bulk to atomic layers. *RSC Advances*, 5, 7495–7514. https://doi.org/10.1039/c4ra11852a

Sundaram, R. S., Engel, M., Lombardo, A., Krupke, R., Ferrari, A. C., Avouris, P., & Steiner, M. (2013). Electroluminescence in single layer MoS2. *Nano Letters*, 13, 1416–1421. https://doi.org/10.1021/nl400516a

Thakurta, S. R. G., & Dutta, A. K. (1983). Electrical conductivity, thermoelectric power and hall effect in p-type molybdenite (MoS2) crystal. *Journal of Physics and Chemistry of Solids*, 44(5), 407–416. https://doi.org/10.1016/0022-3697(83)90068-9

Tomonaga, S. (1950). Remarks on Bloch's method of sound waves applied to many-fermion problems. *Progress of Theoretical Physics*, 5, 544–552. https://doi.org/10.1143/ptp/5.4.544

Tongay, S., Zhou, J., Ataca, C., Lo, K., Matthews, T. S., Li, J., Grossman, J. C., & Wu, J. (2012). Thermally driven crossover from indirect toward direct bandgap in 2D semiconductors: MoSe2 versus MoS2. *Nano Letters*, 12(11), 5576–5580. https://doi.org/10.1021/nl302584w

Van der Waals, J. D. (1893). *Thermodynamische Theorie der Capillarität*. Verh. Kon. Acad.

Wazir, M. B., Daud, M., Safeer, S., Almarzoogi, F., & Qurashi, A. (2022). Review on 2D Molybdenum Diselenide (MoSe2) and its hybrids for green hydrogen (H2) generation applications. *ACS Omega*, 7(20), 16856–16865. https://doi.org/10.1021/acsomega.2c00330

Yadav, R., Sharma, A. K., & Sharma, S. (2025). *Advance Development in Natural Graphite Material and Its Applications: A Review. Mining, Metallurgy and Exploration*, 42(1), 361–385. https://doi.org/10.1007/s42461-024-01167-z

Yao, S., & Wang, Z. (2018). Edge states and topological invariants of non-Hermitian systems. *Physical Review Letters*, *121*, Article 086803. https://doi.org/10.48550/arXiv.1803.01876

Yun, W. S., Han, S. W., Hong, S. C., et al. (2012). Thickness and strain effects on electronic structures of transition metal dichalcogenides: 2H-MX2 semiconductors (M=Mo, W; X=S, Se, Te). *Physical Review B*, 85(3), Article 033305. https://doi.org/10.1103/PhysRevB.85.033305

Yurov, V. M., Goncharenko, V. I., & Oleshko, V. S. (2023a). Study of primary nanocracks of atomically smooth metals. *Journal of Technical Physics Letters*, *49*(8), 35–38. https://doi.org/10.21883/PJTF.2023.08.55136.19504

Yurov, V. M., Goncharenko, V. I., Oleshko, V. S., & Ryapukhin, A. V. (2023b). Calculating the surface layer thickness and surface energy of aircraft materials. *Inventions*, 8(66), 2–15. https://doi.org/10.3390/inventions8030066

Yurov, V., & Zhangozin, K. (2023c). Some questions of the theory of solution viscosity. *German International Journal of Modern Science*, 71, 34–41. https://doi.org/10.5281/zenodo.10460120

Yurov, V., & Zhangozin, K. (2023d). Surface layer thickness, defects and strength of graphite. *The scientific heritage*, 128, 20–27. https://doi.org/10.5281/zenodo.10468004

Yurov, V. M., Goncharenko, V. I., & Oleshko, V. S. (2024a). Deviations from the Wiedman-Franz law. In *International Conference "Scientific research of the SCO countries: synergy and integration"* (6, pp. 203–209). https://doi.org/10.34660/INF.2024.27.51.198

Yurov, V. M., Goncharenko, V. I., Oleshko, V. S., & Zhangozin, K. N. (2024b). Quantum structure of the surface layer of metals. *Herald of Al-Farabi KazNU*, 3(90), 93–107. https://doi.org/10.26577/RCPh.2024v90i3-012

Yurov, V. M., & Zhangozin, K. N. (2024c). At the mechanism of graphite splitting by aqueous solutions. *Znanstvena misel journal*, 86, 41–49. https://doi.org/10.5281/zenodo.10575813

Yurov, V. M., & Zhangozin, K. N. (2024d). On the question of stone–weles defects in grapheme. *International Independent Scientific Journal*, 58, 42–53. https://doi.org/10.5281/zenodo.10492440

Yurov, V. M., Zhangozin, K. N., & Kargin, D. B. (2024e). Crack model in graphene concrete. *Norwegian Journal of Development of the International Science*, 139, 65–69. https://doi.org/10.5281/zenodo.13619789

Yurov, V. M., Zhangozin, K. N., & Kargin, D. B. (2024f). Surface layer of YBCO crystals. *German International Journal of Modern Science*, *88*, 51–58. https://doi.org/10.5281/zenodo.13786008

Yurov, V. M., Goncharenko, V. I., Oleshko, V. S., & Zhangozin, K. N. (2025a). Open quantum system of the surface layer of atomically smooth metals. *Journal of Applied and Fundamental Sciences*, 4, 52–57. https://doi.org/10.17513/mjpfi.13720

Yurov, V. M., Zhangozhin, K. N., & Kargin, D. B. (2025b). Fermi energy of graphite monolayers. In *X International Scientific-Practical Conference: March 5-7* (pp. 75–82). Stockholm, Sweden. http://www.regionacadem.org

Yurov, V. M., Zhangozin, K. N., & Kargin, D. B. (2025c). Quantum structure of the surface layer of graphite. *Endless light in science*, 2025(1), 206–212. https://doi.org/10.24412/3007-8946-2025-31-206-212

Yurov, V. M., Zhangozin, K. N., Portnov, V. S., Rakhimova, G. M., & Rakhimov, A. M. (2025d). Concrete reinforced with graphene and graphene oxide. *Material and Mechanical Engineering Technology*, 1, 36–42. https://doi.org/10.52209/2706-977X_2025_1_36

Yurov, V. M., Zhangozin, K. N., Zhanabergenov, T. K., & Kargin, D. B. (2025e). On the issue of warping of graphene layers. *Herald of D. Serikbayev EKSTU*, 1, 101–113. https://doi.org/10.51885/1561-4212_2025_1_101

Zhang, M., Wu, J., Zhu, Y., Dumcenco, D., Hong, J., . . . Xie, L. (2015). Two-dimensional molybdenum tungsten diselenide alloys: Photoluminescence, Raman scattering, and electrical transport. *ACS Nano*, 8(7), 7130–7137. https://doi.org/10.1021/nn5020566

Zhang, T. (2022). *Graphene. From theory to applications*. Springer.

Zhong, F., Ye, J., He, T., Zhang, L., Wang, Z., & Li, Q. (2021). Substitutionally doped MoSe2 for high-performance electronics and optoelectronics. *Small*, 17, Article 2102855. https://doi.org/10.1002/smll.202102855

Zhu, Q., & Mayer, W. G. (1993). On the crossing points of Lamb wave velocity dispersion curves. *Journal of the Acoustical Society of America*, 93(4), 1893–1895. https://doi.org/10.1121/1.405679

Zoraghi, M., Barzola-Quiquia, J., Stiller, M., Setzer, A., Esquinazi, P., Kloess, G., Muenster, T., Lühman, T., & Estrela-Lopis, I. (2017). Influence of rhombohedral stacking order in the electrical resistance of bulk and mesoscopic graphite. *Physical Review B*, 95, Article 045308. https://doi.org/10.1103/PhysRevB.95.045308

Отримано редакцією журналу / Received: 28.11.25
Прорецензовано / Revised: 30.12.25
Схвалено до друку / Accepted: 18.02.26
Опубліковано / Published: 27.02.26

Віктор ЮРОВ[1], д-р техн. наук, проф.
ORCID ID: 0000-0002-7918-9656
e-mail: s.imanbaeva1@ktu.edu.kz

Василь ПОРТНОВ[2], д-р техн. наук, проф.
ORCID ID: 0000-0002-4940-3156
e-mail: v.portnov@ktu.edu.kz

Сергій ВИЖВА[3], д-р геол. наук, проф., чл.-кор. НАН України
ORCID ID: 0000-0003-4091-6649
e-mail: s.vyzhva@knu.ua

Микола РЕВА[3], канд. фіз.-мат. наук, доц.
ORCID ID: 0009-0009-1307-7617
e-mail: mvreva@gmail.com

Канат ЖАНГОЗІН[2,4], канд. фіз.-мат. наук, доц.
ORCID ID: 0000-0003-1234-0486
e-mail: s.asylzat@ktu.edu.kz

Андрій ГОЛІК[2], асп.
ORCID ID: 0009-0008-5179-0002
e-mail: andrey.golik@i-geo.kz

[1]ТОВ "ТБК-Схід", Караганда, Казахстан
[2]Карагандинський технічний університет ім. А. Сагінова, Караганда, Казахстан
[3]Київський національний університет імені Тараса Шевченка, Київ, Україна
[4]ТОВ "Схід", Астана, Казахстан

ПОВЕРХНЕВИЙ ШАР ШАРУВАТИХ МІНЕРАЛІВ

В с т у п . ***Поверхневий шар мінералів графіту, дисульфідів і диселенідів молібдену являє собою ультратонку плівку товщиною від ~2 нм у площині шарів до ~6 нм перпендикулярно до цих шарів. Ця плівка містить: для графіту – 3 моношари, для MoS_2 – 4 моношари, для $MoSe_2$ – 5 моношарів. Поверхневий шар мінералів таких розмірів є 2D-структурою, яка відмінна від об'ємного (масивного) кристала. Всі наношари цього шару також відмінні один від одного через наявність розмірних ефектів. Метою даної роботи є дослідження квантової структури поверхневого шару зазначених мінералів, установлення відмінності металів і напівпровідників, дослідження пов'язаних з поверхневим шаром таких явищ, як електрична провідність мінералів і перетворення енергії деформації внаслідок реконструкції їх поверхні. На основі представлення наношарів мінералів як квантових ниток, результатів раніше виконаних авторських робіт та викладених у наукових публікаціях результатів досліджень інших учених, виконано відповідні аналітичні розрахунки, що дають змогу досягти сформульованих вище цілей.***

Р е з у л ь т а т и . ***Було встановлено, що при зменшенні товщини напівпровідників електрична провідність зростає, що протилежно до поведінки, яка спостерігається в металах. Зокрема, провідність поверхневого шару графіту на два порядки, а дисульфіду та диселеніду молібдену (MoS_2 і $MoSe_2$) на чотири порядки вища за провідність об'ємної фази цих мінералів. Виявилося також, що за своїми електронними властивостями графен знаходиться посередині між звичайними металами і напівпровідниками. У статті показано, що квантові нитки в наношарі взаємодіють між собою, що відповідає квантовій заплутаності ферміонів як спінової системи. Показано, що енергія деформації, що пов'язана з реконструкцією поверхні мінералів, визначає фізичні властивості як наношару, так і об'ємного кристала; її знання відкриває шлях до аналізу таких фізичних властивостей: явище термо-ЕРС (робота термопари); термоелектричні ефекти (Зеєбека, Пельтьє, Томсона); робота виходу електронів; теплоємність та ін. Розглянуто перетворення енергії деформації у різні види енергії. Показано, що енергія деформації при зовнішньому впливі витрачається на акустоемісію (поширення звукових хвиль), автоелектронну емісію (випромінювання повільних електронів), фрактолюмінесценцію та на тепловиділення (під час тертя).***

В и с н о в к и . ***Поверхневий наношар мінералів R(l) є відкритою квантовою системою, у якій виявляються квантові розмірні ефекти, що призводять до аномальних фізичних явищ. Енергія деформації, що виникає в мінералах при реконструкції поверхні, відображає всі суттєві властивості об'ємних мінералів, що мають важливе практичне значення: акустичні властивості матеріалів, необхідні для неруйнівного контролю якості і виявлення механізмів руйнування; автоелектронну емісію носіїв заряду з металевих та напівпровідникових структур, критично важливу для мікро- та наноелектроніки, фотоніки та інших технологічних додатків; процес фрактолюмінесценції в мінералах, що розкриває механізми тертя в шаруватих мінералах та потенційні шляхи надання їм супермастильних властивостей. Цей перелік практичних застосувань, пов'язаних з енергією деформації, що генерується в мінералах при реконструкції поверхні, може бути розширений. Таким чином, формується новий напрямок наукових досліджень – фізика поверхневого шару твердих тіл та рідин (зокрема, для води R(l)=1,1 нм).***

К л ю ч о в і с л о в а : ***мінерал, поверхневий шар, наношар, мезошар, об'ємна фаза, провідність, квантові нитки, енергія деформації, енергія Фермі.***

Сергій Вижва є головним редактором видання, тому не брав участі у рецензуванні та прийнятті рішення щодо публікації цієї статті.

Автори заявляють про відсутність конфлікту інтересів. Спонсори не брали участі в розробленні дослідження; у зборі, аналізі чи інтерпретації даних; у написанні рукопису; в рішенні про публікацію результатів.

Serhii Vyzhva is the editor-in-chief, therefore did not take part in the peer-review process or in the decision to publish of this article.

The authors declare no conflicts of interest. The funders had no role in the design of the study; in the collection, analyses or interpretation of data; in the writing of the manuscript; or in the decision to publish the results.